Jefferson Lab

Newport News, VA

*GlueX/Hall D Calorimeter Final Design and Safety Review*
**February 19-20, 2008**


# Section 5:
# Calorimeter Simulation and Reconstruction

GlueX/Hall D Calorimeter Conceptual Design Report
*Section 5 of 5*

# 5 Calorimeter Simulation and Reconstruction

A key aspect of detector design is the development of accurate simulation and reconstruction algorithms. A full detector simulation allows one to make informed decisions about detector design before construction begins. In addition, simulation of the detector response allows one to begin to develop reconstruction algorithms and a physics analysis framework that will be valuable once data taking begins. Finally, an accurate simulation of the detector is an important analysis tool in that it permits an accurate calculation of the acceptance, a critical input to amplitude analysis. In this section we present progress on simulation and reconstruction efforts in order to evaluate and validate the performance of the barrel and forward calorimeters.

## 5.1 Overview

A schematic diagram of the data flow for the full calorimeter simulation and reconstruction framework is shown in Figure 5.1. The items in standard text represent software packages that have been developed and tested, while algorithms that need to be implemented are underlined. The full simulation and reconstruction chain for neutral particles has been developed, while high-level interfaces to tracking and full event fitting need further development. The software package has been written in the context of a larger, experiment-wide analysis framework so that it can be used directly in physics analysis when data become available. In what follows we provide an overview of the simulation and reconstruction algorithms which are intended to provide an accurate picture of the expected performance of the calorimeters. We discuss neutral particle reconstruction resolutions and efficiencies and present preliminary results on physics analyses with mock data sets.

## 5.2 Simulation

The simulation starts with the output from a Monte-Carlo (MC) physics generator. The suite of available generators are capable of generating events as simple as single particles with a fixed trajectory and momentum and as complicated as multibody decays with appropriate angular distributions for testing amplitude analysis. In addition an implementation of PYTHIA has been tuned to generate generic hadonic photoproduction events that can be used to assess hadronic backgrounds for specific physics channels. Generated particles are propagated through a full GEANT3-based hit-level detector simulation that includes all active and inactive, *e.g.,* support structures, material within the detector volume. Additional digitization and response effects are incorporated outside of GEANT to produce the equivalent of a raw detector hit.

## 5.3 FCAL simulation

Shower simulation in the FCAL is currently based on a model that takes into account energy deposition of secondary charged particles in the shower via ionization in the lead glass block. Due to computing limitations, it is not practical to simulate optical effects of Čerenkov photons in the lead glass. To mimic the attenuation length in glass, the energy deposited is attenuated by $e^{-\Delta z/\lambda}$ where $\Delta z$ is the distance to the back of the block and $\lambda = 160$ cm.[1] At the MCHit stage (Figure 5.1, the position in $x$-$y$ plane, the block energy $E$ and

[1] This value is the current attenuation length in the simulation and is currently under study.

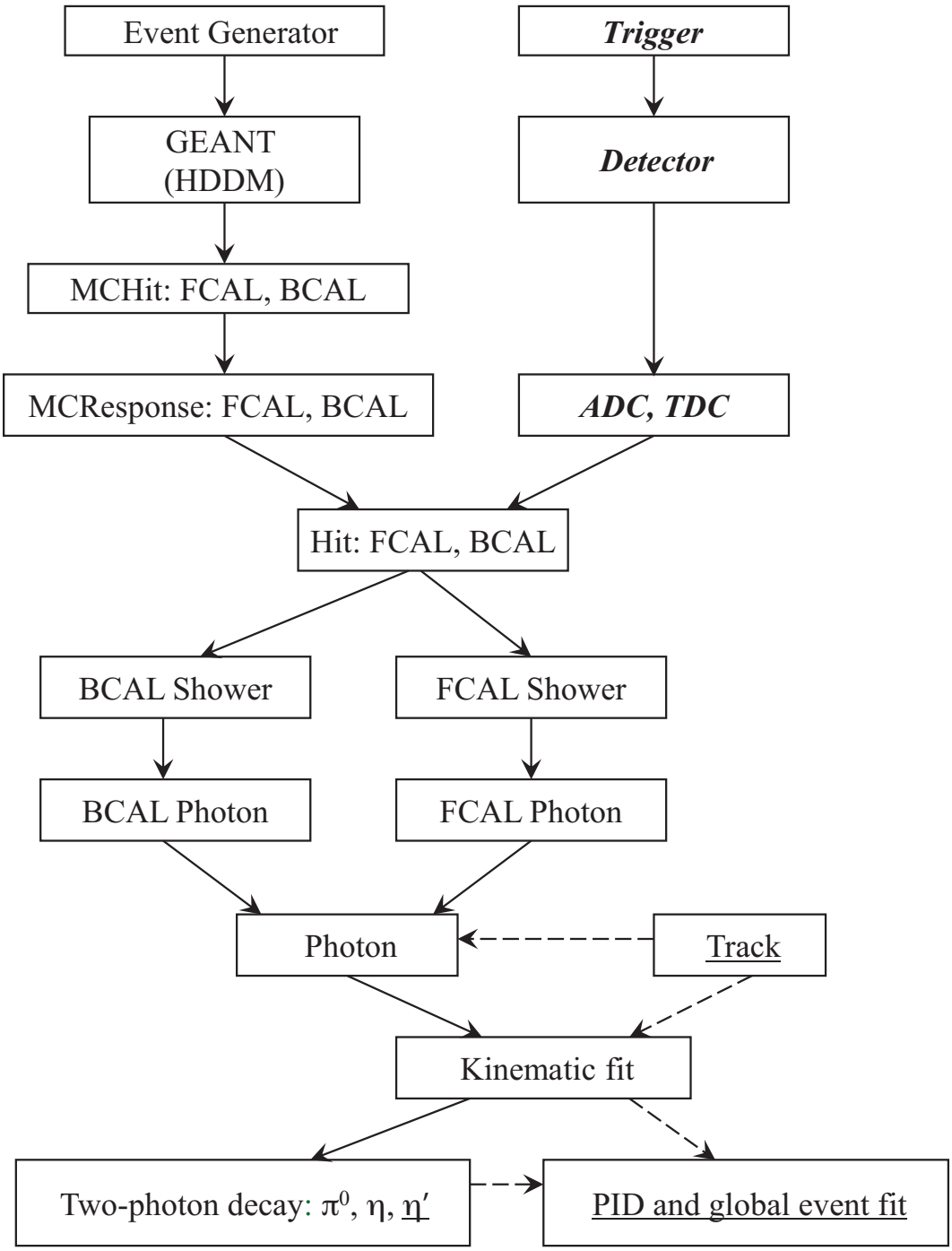


Figure 5.1: Data flow diagram for the GlueX calorimeters. The italicized items are part of the actual data acquisition stream in the experiment. Standard text corresponds to existing and working software, while underlined text indicates algorithms that need implementation or additional development.

time $t$ are saved for subsequent shower reconstruction.

**Photostatistics:** A dominant contribution to the calorimeter resolution is the effect of statistical fluctuations in the number of photonelectrons produced in the PMT. As noted in Section 4 on FCAL, this contribution is minimized by utilizing a light guide configuration that maximizes the transmission of Čerenkov photons into the PMT. Since our simulation is based purely on energy deposition via ionization and does not incorporate optical photon detection, we must introduce an additional degradation of the energy resolution to accurately mimic photostatistical effects. Based on experience with RadPhi and also bench tests with cosmic rays, we add an additional, uniform 3.5% Gaussian smearing to the detected energy. More advanced simulations that incorporate angular dependence of efficiency and Čerenkov photons are under study.

**Electronics threshold:** The detection threshold in each block is an important input to the simulation as it defines what fraction of the shower goes undetected in perimeter blocks around the core of the shower. Studies show that a cosmic ray passing through the transverse (short) dimension of the block produces about as many photoelectrons in the PMT as a 30 MeV photon incident along the axis of the block. As described in Section 4, it is possible to clearly detect signals from cosmic rays passing through the lead glass block. Making conservative assumption that these signals are at the threshold of detection, we discard signals from all blocks that have less than 30 MeV of deposited energy since we assume they would fall below the threshold for detection. This threshold will be refined as we improve our understanding of signal processing using flash ADC electronics. Both photostatistics modeling and the electronics threshold are applied at the MCResponse stage (Figure 5.1).

### 5.3.1 BCAL simulation

The BCAL simulation, like the FCAL simulation, models shower development by tracking secondary charged particles through the active BCAL region and accumulating the deposited energy via ionization. While the material is modeled with the appropriate mixture of lead, scintillator, and epoxy, the fiber geometry and production and collection of scintillating light in the fibers is not modeled as the resulting simulation would be too computational expensive to be practical. Extensive simulations have been and are being performed using a stand-alone GEANT-based software package that models the full Pb/SciFi matrix. The application of this stand-alone software in understanding the response of the BCAL prototype modules in beam and cosmic ray tests and in specifying the readout segmentation are summarized in Appendix C of Section 2 on BCAL. At the MCHit stage (Figure 5.1), the energy weighted average $z$-position and energy weighted average time of all energy deposits (associated with Geant "steps") made in the BCAL cells by secondary shower particles are saved for each segment for further processing[2].

**Sampling fraction fluctuations:** Only about 12% of the volume of the BCAL is filled with scintillator. With a relatively small active volume, statistical variations in the fraction of the shower that is "sampled" by the scintillator degrade the energy resolution and must be taken into account when accurately simulating the calorimeter response. Fluctuations in the sampling fraction are modeled by smearing the signal in each cell by a Gaussian distribution with a width that is a fraction of the mean sampling fraction, $\sigma_f/f$. Based

[2]The BCAL simulations discussed here utilized an earlier version of the segmentation: 4 azimuthal by 5 radial cells for the inner 10 cm in radius and 3 azimuthal by 4 radial cells for outer portion of the end of each module. While we plan to implement and study this new segmentation in the future, we expect only minor changes in performance as the cell size in the heavily populated inner layers remains unchanged.

on independent Monte Carlo study [1], sampling fraction fluctuations depend on energy deposited in a cell as

$$\frac{\sigma_f}{f} = \frac{A}{\sqrt{E_{\text{dep}}}} + B, \tag{5.1}$$

with A and B being 4.22% and 1.29% respectively. After the sampling fraction fluctuations are applied, the signal is propagated to the downstream and upstream readout ends. This preserves the end-to-end correlation in the sampling fraction fluctuations. Energy attenuation and time delay are implemented by using effective attenuation length $\lambda = 300$ cm and speed of light in the fiber $c' = 16.75$ cm/ns[3].

**Electronics threshold:** To reduce data volume, the outputs of photo-sensing devices are zero-suppressed. Since this effectively removes segments with low energy around the borders of a shower, the same zero-suppression must be applied in the Monte Carlo in order to model the resolution of the detector. This electronics threshold is a strong function of the choice of readout device, light output of the scintillating fibers, and desired zero-suppression factor.

In estimating the threshold to use in the simulation, it was assumed that the competition between the relatively high dark rate of the SiPM devices and the desire for low occupancy (assumed to be $< 5\%$) would ultimately set the threshold. Based on the design specifications for the SiPM devices, the following method was used to estimate the electronics threshold. Given a 60 MHz dark rate, the probability to have 11 or more dark pulses in a single 100 ns window is about 4%, so we take 11 photoelectrons as the threshold. To reach 11 photoelectrons 286 keV of deposited energy in the fibers is needed, or, assuming a sampling fraction of 12%, 2.4 MeV of energy in the cell after attenuation. After sampling fraction smearing and attenuation procedures described above, all hits which are less than 2.4 MeV are removed.

### 5.3.2 Simulation improvements

While we believe the dominant contributions to photon detection efficiency and resolution are appropriately modeled in the simulation, there are additional errors in digitization and response that are not currently modeled, including:

- injection of SiPM dark noise into MC;
- smearing due to statistical fluctuations in BCAL photosensors;
- smearing that degrade the timing resolution of hits in FCAL and BCAL; and
- smearing due to electronics digitization of the signals such as limited precision due to the size of the least count in both the ADC and TDC.

As these effects are studied and consequently better understood, they will be incorporated into the simulation. However, we do not expect substantial deviation from the current simulated performance.

[3] As these parameters are better understood through studies as described in previous simulation, we will continue to revise and improve our model.

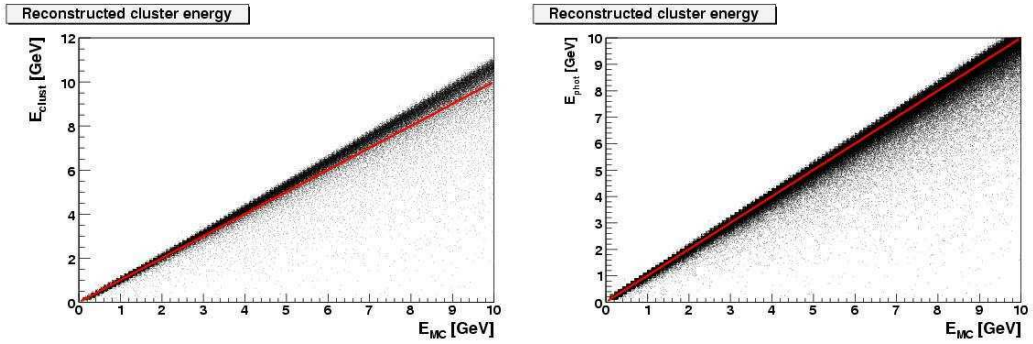


Figure 5.2: Reconstructed cluster energy as a function of generated energy before (left) and after (right) the non-linear energy corrections. Solid red lines correspond to $E_{\text{reconstructed}} = E_{\text{generated}}$.

## 5.4 Photon reconstruction

To study single photon reconstruction, photons were generated at the center of the target and thrown uniformly in azimuth and polar angle to examine the full coverage of the FCAL and BCAL. Hits in each of the calorimeters are grouped into clusters using algorithms specific to each detector. Because of non-linear effects, like signal attenuation or shower leakage, the cluster energies and positions are then calibrated to match the generated photon momentum. In addition, a detector dependent error matrix is formed for each photon, which is subsequently used by a kinematic fitter to perform mass-constrained fits of pairs of photons to $\pi^0$ and $\eta$ hypotheses.

### 5.4.1 FCAL reconstruction

The reconstruction algorithm for FCAL photons is based on that used for the RadPhi experiment [2, 3]. The algorithm groups FCAL hits into clusters through an iterative process that starts by selecting the highest energy block. Showers have a radial profile that consists of two parts: a core that drops with the distance from the seed block as a fourth-order exponential function and a logarithmically decreasing tail. A portion or all of the energy in other hit blocks within a 25 cm radius is then added to the cluster according to this profile. The process continues with a new seed from the remaining blocks until are blocks are assigned to a cluster. A minimum of two blocks are needed to form a cluster which sets the threshold for photon detection in the range of 60-100 MeV. After the clusters are formed, the cluster energy and position is corrected for known shower depth and non-linear effects.

**Energy and depth corrections:** The reconstructed cluster energy as a function of generated photon energy is shown in Figure 5.2. The plots ware obtained by generating single photons uniformly in full azimuth, from 0-12° in polar angle and with energy between 0 and 10 GeV. For the sake of accurate calibration, it was also required that photons do not convert into $e^+e^-$ pairs in the material in front of the FCAL. The plot on the left was obtained after simply scaling the cluster energy to match 1 GeV photons. Deviation from a straight line (red) due to the non-linear energy response of the FCAL is evident.

There are two competing processes that have opposite effects on the observed non-linear energy response:

(1) simulated attenuation of Čerenkov photons, which is dominant for low energy showers, and (2) shower leakage, which affects high energy showers. When the photon energy increases, the core of the shower moves towards the downstream face of the FCAL and reduces attenuation. This increases the relative gain of higher energy photons with respect to low energy photons. However, when the shower leakage at the back of the block starts to play a role it has a reverse effect on the relative gain of energetic photons. The final result is that the energy non-linearity varies weakly with shower energy. This small energy dependence is neglected and a constant non-linear factor $\epsilon = 0.035$ was used to reconstruct photon energy $E_\gamma$ from cluster energy, $E_c$, by fitting data from the left plot in Figure 5.2 to the following form

$$E_c = N \cdot E_\gamma^{1+\epsilon}. \tag{5.2}$$

The normalization factor, $N = 0.65$, in the above equation depends mainly on the effective attenuation length in the lead glass. The reconstructed photon energy after applying the non-linear correction is shown in the right plot of Figure 5.2.

In order to reconstruct the incident polar angle $\theta$, one needs to know the shower position along the $z$-axis, which cannot be obtained from the response of the FCAL blocks (see Fig 5.3). The shower depth has a logarithmic dependence on energy while energy non-linearity also depends on shower polar angle due to leakage and optical effects. For the small polar angles covered by the FCAL, we neglect this correlation between angle and energy non-linearities. Using the formula for the average shower depth at normal incidence: [4]

$$z_A = X_0 \left[ ln\left(\frac{E}{E_c}\right) + C_0 \right], \tag{5.3}$$

where $X_0$ represents the radiation length, $E_C$ is the critical electron energy, and $C_0$, the shower offset, depends on the material and whether the shower is photon or electron induced. One can then write the first order approximation for the $z$-position as

$$z = z_0 + z_A \cos\theta, \tag{5.4}$$

where, $z_0$ is the distance from the interaction point to the forward face of the FCAL, and

$$\tan\theta = \frac{r_0}{z_0 + z_A \cos\theta_0}, \tag{5.5}$$

$$\tan\theta_0 = \frac{r_0}{z_0}, \tag{5.6}$$

where the subscript zero represents the apparent position or angle on the face of the of the wall (see Figure 5.3). In the range of angles relevant for the GlueX experiment, the above first order correction to the polar angle appears to be sufficient.

**Energy and position resolution:** Figure 5.4 shows photon energy resolution as a function of generated energy after non-linear energy and depth corrections were applied. The energy resolution was fitted by the standard form

$$\frac{\sigma_E}{E} = \frac{A}{\sqrt{E}} + B, \tag{5.7}$$

with negligible floor term $B$ and statistical term $A$ of $\approx 5.7\%$. We note that the statistical term is consistent with what is expected based on light guide simulations discussed in Section 4. Figure 5.5 shows the absolute error in polar (left) and azimuthal (right) angle vs. generated polar angle. The error in polar angle does not depend on actual shower position at the face of the FCAL. In the case of $\phi$, one can see the effect of the finite FCAL block size at small polar angles.

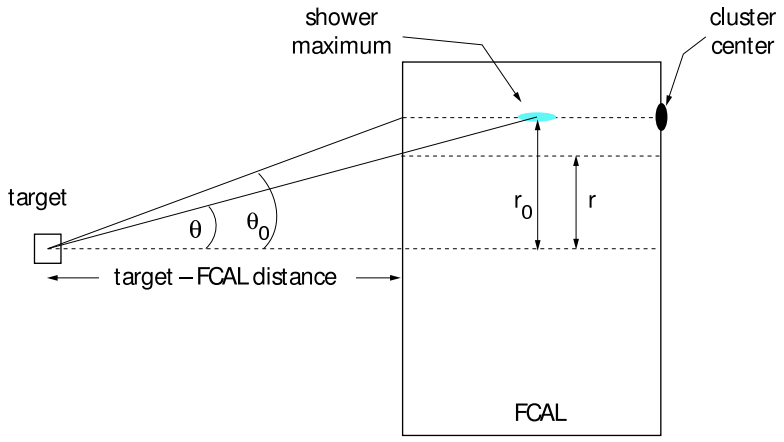


Figure 5.3: Diagram that shows shower-depth and polar angle relation to the measured cluster centroid.

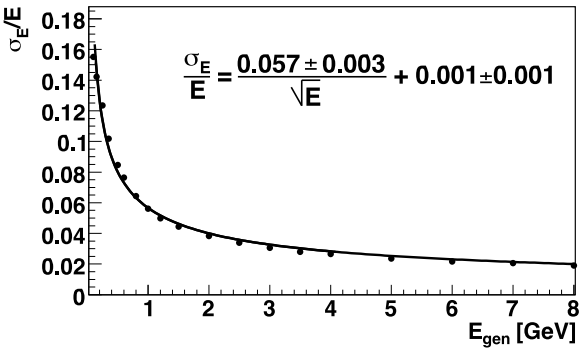


Figure 5.4: Fractional energy resolution as a function of generated energy after energy-corrections were applied.

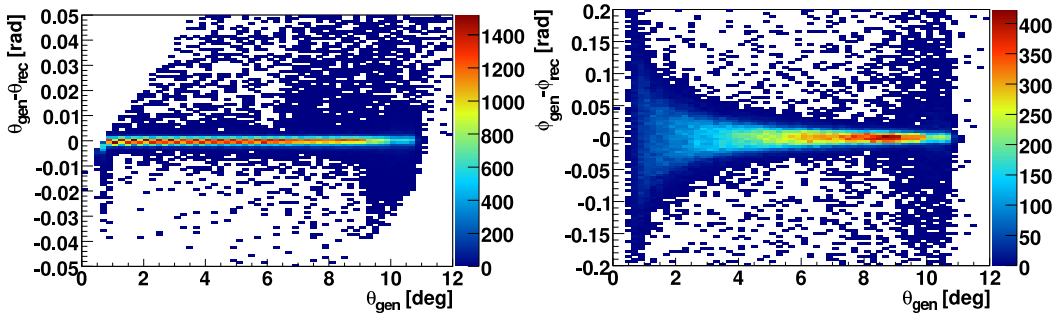


Figure 5.5: Polar (left) and azimuthal (right) angle errors vs. generated polar angle after energy/depth corrections were applied.

Overall, the achieved efficiency for reconstructing single FCAL showers from photons that did not convert before reaching the FCAL is $> 99.5\%$. The small fraction of single photons that are not reconstructed consists of so-called split clusters, where shower fluctuations cause the clustering algorithm to reconstruct one photon as two.

### 5.4.2 BCAL reconstruction

The shower reconstruction for the BCAL is based on the algorithm developed for the KLOE calorimeter [5]. The algorithm converts upstream and downstream readout signals to single cell hits that are characterized by $(x, y, z)$ position, energy $E$, and average time $t$, where the $z$ position is calculated by the end-to-end time difference taking the effective speed of light of 16.75 cm/ns. The cell energy has been corrected for attenuation based on the value of $z$. The algorithm then does a purely geometrical clustering of hits by grouping neighboring cells, with no consideration to energy deposition or shower profile. Clusters separated less than 40 cm in space, 30 cm along $z$ and 2.5 ns in time are merged. Clusters are split in $z$ direction if their r.m.s time is greater 5.0 ns. After the cluster merging and breaking routines, final energy-weighted spatial positions for the showers are determined. To avoid creation of spurious clusters due to isolated low energy cells in the calorimeter, all showers with energy less than 20 MeV are removed.

As a final step in the reconstruction algorithm, the 3D energy-weighted position within a layer for each cluster is determined. These 3D points are projected onto the $x$, $y$, and $z$ axis and fit to lines so that a parametric representation of the path of the photon can be inferred. One can parametrically write the trajectory of the photon as a function of some parameter, $s$, as

$$\mathbf{d}(s) = \mathbf{a} + s\mathbf{c}. \tag{5.8}$$

The vectors $\mathbf{a}$ and $\mathbf{c}$ (and their errors) represented a point on the trajectory and the direction of the photon, respectively, and are determined by the series of linear fits. Ideally $\mathbf{c}$ should be parallel to the photon momentum, and, by construction of the fit, $\mathbf{a}$ will be the point where the photon struck the BCAL inner surface. Currently the vector pointing from the target to $\mathbf{a}$ is taken as the photon momentum[4]. The errors on $\mathbf{a}$ are used in forming the photon error matrix (see Sec. 5.4.3).

**Energy correction:** To calibrate the reconstructed photon energy, the detector was uniformly populated in $z$ and azimuth with photons that have an energy between 0 and 2 GeV. All photons are thrown from the center of the target and only those photons that did not convert before reaching the BCAL are considered.

For the events when exactly one BCAL shower was reconstructed, the ratio of reconstructed to generated energy for two different slices in $z$ is shown in Figure 5.6. One can see the non-linear energy response that depends on the $z$-position of the incident photon. Equation 5.2 can be used to correct reconstructed shower energy to match incident photon energy. The fit with $N$ and $\epsilon$ as free parameters is shown in Figure 5.6 by solid blue line. Both the normalization $N$ and non-linear factor $\epsilon$ depend on $z$-position, and these dependencies are extracted to determine the calibration.

**Energy and position resolution:** The characteristic resolution of the BCAL was examined using only photons incident in the $z$-region of 30 cm $< z <$ 380 cm, avoiding the regions near the upstream and

[4]Note that the reconstruction algorithm provides the possibility to determine the trajectory of the photon *without* the assumption that it originates target. We are currently not utilizing this technique as the systematic uncertainties associated with it have not been fully explored.

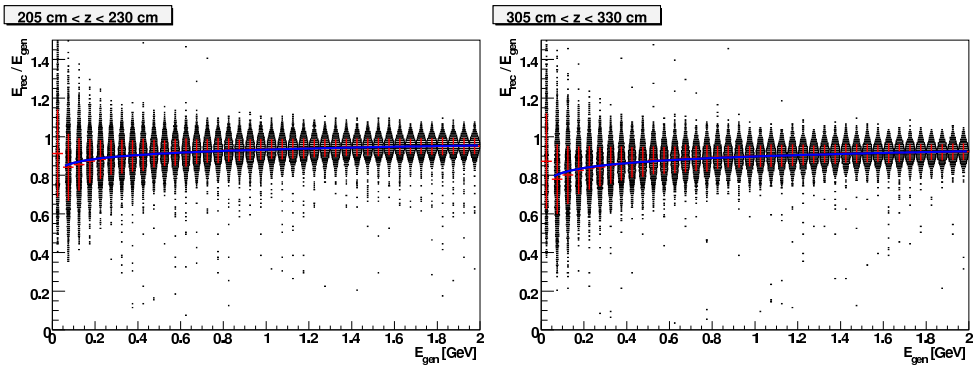


Figure 5.6: Energy dependence of the ratio of the reconstructed to generated energy for two ranges in z position of incident photons. Data are shown in boxes with an overlaid (red) profile plot. The fit for the region greater than 50 MeV is of the form given by Equation 5.2. The region below 50 MeV was excluded from the fit because of the bias from large sampling fraction fluctuations for clusters consisting only of low energy cells.

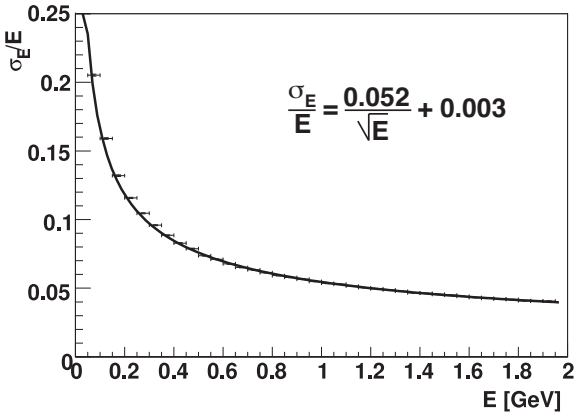


Figure 5.7: A fit to the standard deviation of the fractional energy error, $\sigma_E/E$ as a function of energy.

downstream ends of the BCAL where leakage is excessive. Figure 5.7 gives the characteristic energy resolution of the BCAL and is fit to a function of the form given by Equation 5.7. The statistical $A$ and floor $B$ terms are 5.4% and 0.3%, to be compared to what was obtained in the BCAL test beam analysis: $A = 5.5\%$ - $6.1\%$ and $B = 1.6\%$ - $2.4\%$, depending on analysis method.

Figure 5.8 shows both the absolute error in polar angle and photon impact $z$ position as a function of $z$. The observed structure in the peak height as a function of $z$ is due to efficiency variation. Errors in polar angle can be written in terms of the $z$-position error as

$$\delta\theta = \frac{r}{z^2 + r^2}\delta z. \tag{5.9}$$

One notices from Figure 5.8 that while the z resolution degrades as one moves downstream due to dispersion of the shower along the BCAL axis the polar angle resolution still improves because of the $z^2$ factor in the denominator in RHS of the expression above. Given the speed of light in fibers is roughly 17 cm/ns, position

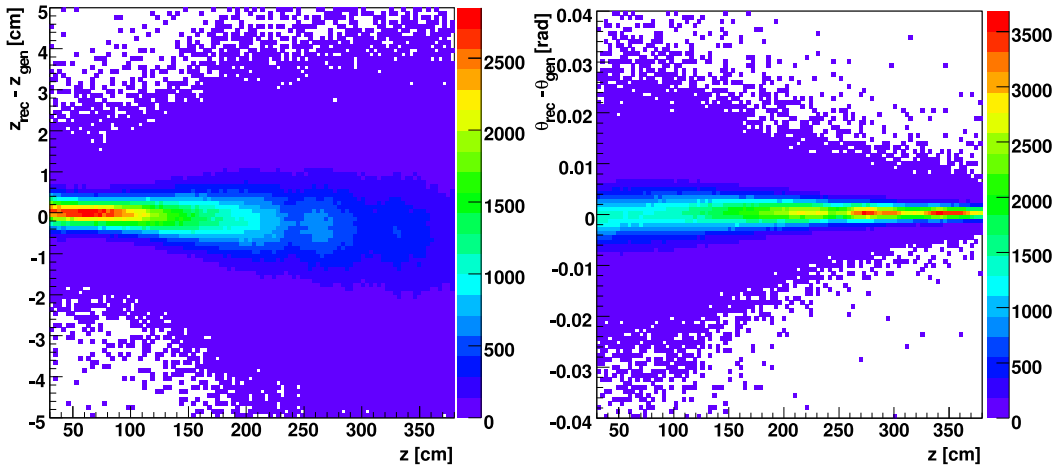


Figure 5.8: Absolute reconstruction error in $z$ position of photon impact point (left) and polar angle (right) as a function of $z$ position of photon impact point.

resolutions on the order of a couple of millimeters, as indicated in the plots, will degrade and become more realistic when an accurate model of the timing resolution is implemented.

The resolution in azimuthal angle, $\phi$, is derived from the shower position in the transverse plane, which is related to the energy-weighted average position of the cells the cluster. Unlike polar angle resolution, azimuthal angle resolution does not depend on timing information and therefore we expect it to be accurately modeled by simulation. Figure 5.9 shows the absolute error in $\phi$ for photons evenly distributed in $z$ and in energy between 0 and 2 GeV. The characteristic resolution obtained from this plot of 5.6 mrad is slightly better than the stated design goal of 8.5 mrad.

Overall, the energy resolutions obtained from MC simulations of both calorimeters are slightly better than expectation based on past experience and beam tests. Most notably, the resolutions appear to be purely statistical – no significant floor term is apparent in the MC modeled resolution. This is likely due to the inability for the simulation to accurately model additional and potentially unkown systematic effects that may degrade the resolution. Continued study of simulation and beam test data may provide an opportunity to both improve the accuracy of the modeled resolution and understand systematic errors in reconstruction of data.

### 5.4.3 Photon kinematics and covariance matrix

The photon reconstruction algorithms for both the BCAL and FCAL measure the shower position $\mathbf{r}_c$ and energy $E_c$ in the calorimeter. They can be transformed into properties of the photon using:

$$E_\gamma = E_c, \tag{5.10}$$

$$\mathbf{p}_\gamma = \frac{E_\gamma}{|\mathbf{r}|}\mathbf{r}, \tag{5.11}$$

where $\mathbf{r} = \mathbf{r}_c - \mathbf{r}_v$ with $\mathbf{r}_v$ representing the vertex position. The vertex position will ultimately be measured by finding the origin of charged particle tracks. Currently the vertex is assumed to be at the center of the target with errors given by the size of the target.

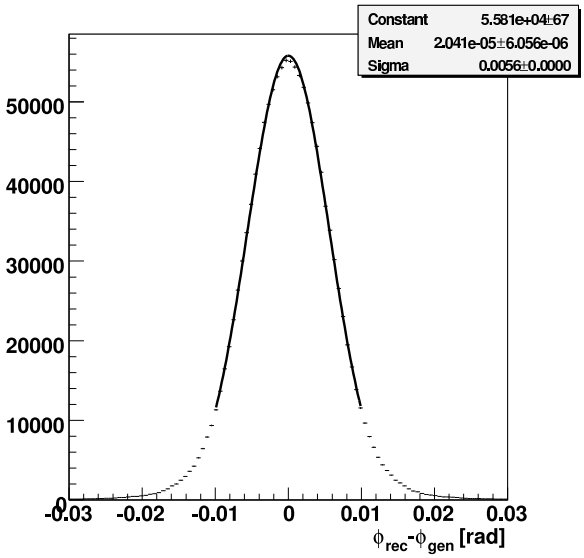


Figure 5.9: Distribution of absolute error in azimuthal angle reconstruction. The data are well described by a Gaussian with $\sigma = 5.6$ mrad.

Calorimeter dependent energy error $\sigma_E$ is given by Equation 5.7. The statistical terms $A$ for the BCAL and FCAL are 5.2% and 5.7% respectively, while the floor term $B$ is less than 0.3% for both detectors. As a first approximation for position errors, it is assumed that photon position and energy are measured independently[5]. Errors on shower position in the BCAL are determined during shower reconstruction from the fit of the photon impact point at the inner BCAL radius. Thus, $\sigma_{r_i} = \delta a_i$, where $\mathbf{a}$ is defined by Equation 5.8. In the case of the FCAL, the errors on the $x$ and $y$ positions of the cluster are set to the average position error of 0.7 cm, and the error along $z$ is taken as the difference between the zero and first approximation in calculating shower depth.

Using these errors, one can construct the diagonal covariance matrix for the measured detector quantities. The expressions for the photon energy and momentum in terms of these detector quantities are used to construct the Jacobian to transform this covariance matrix into the coordinate system that spans $E_\gamma$ and $\mathbf{p}_\gamma$. The representation of the photon covariance matrix in this coordinate system is then a suitable input to a kinematic fitter that is capable of performing mass-constrained fits of pairs of photons to reconstruct decays of $\eta$ and $\pi^0$ mesons.

### 5.4.4 Reconstruction efficiency

A serious issue that affects the efficiency of the calorimeters is the conversion of photons into $e^+e^-$ pairs in the material between the interaction point and the calorimeter. Since our simulation incorporates all material within the volume of the the GlueX detector, we can accurately study this effect.

Fig 5.10 (top) shows photon conversion probability between the target and one of the calorimeters. The central (CDC) and forward (FDC) drift chambers were identified as large contributors to photon conversion

[5]The weak dependence of shower depth in the FCAL on energy can be neglected.

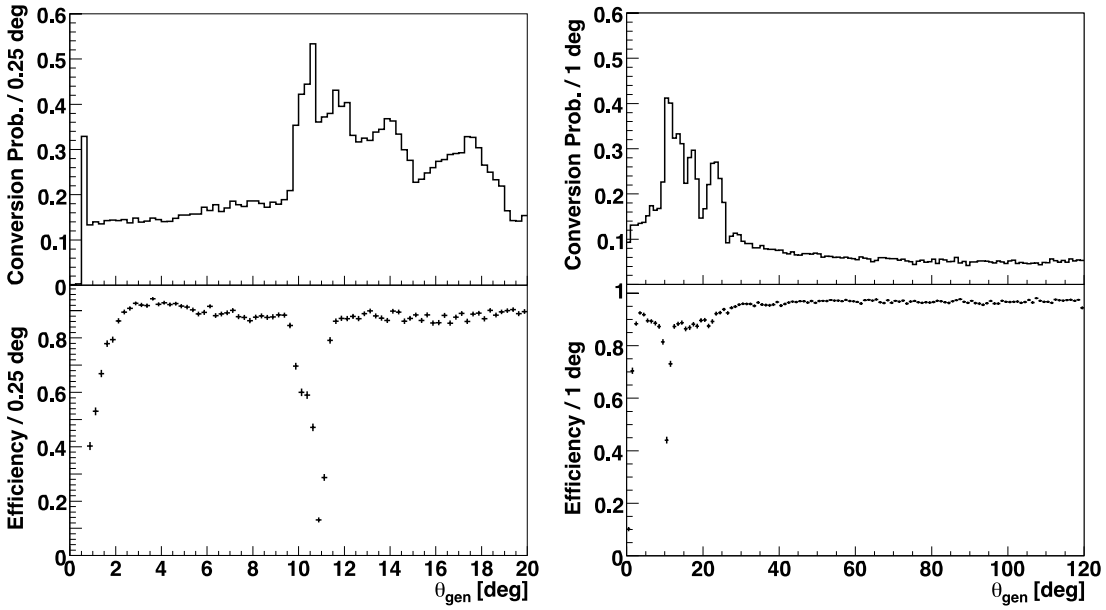


Figure 5.10: Top: Single photon conversion probability as a function of incident polar angle. A spike at angle below 1° on the left plot is the beam-hole effect, while CDC endplate and FDC support rings can be identified by the steps in conversion probability. Bottom: Single photon reconstruction efficiency as a function of incident polar angle. All plots are generated for 1 GeV photons.

that degrades photon reconstruction efficiency and resolution in the forward region. Material in the support frames and active regions of these detectors has been reduced where possible to minimize efficiency loss.

The actual photon detection efficiency is not the inverse function of the conversion probability, because in some cases, photon conversion still leads to reconstruction of one shower that preserves incident photon momentum. This is true, for example, in the forward time-of-flight (TOF) detector, where a converted photon does not produce two separate showers in the FCAL. Additional material in front of the FCAL, including a Plexiglas sheet for distribution of calibration signals and a light tight cover for the front of the FCAL does not degrade FCAL performance.

A plot of the photon reconstruction efficiency is shown in Figure 5.10 (bottom) for polar angles covered by the two calorimeters. The plot includes all reconstructed photons within $3\sigma_E$ of the generated energy and within 0.05 rad of generated angle. The energy error $\sigma_E$ is given by the energy resolution the appropriate calorimeter. The plot on the left shows the efficiency in a region of polar angle where reduced acceptance is expected. Currently further studies are underway to determine both the impact and reduction of the minimized efficiency in this "gap region" between the forward and barrel calorimeters.

## 5.5 Physics signals

Ultimately we look to simulation to validate the design of the detector and demonstrate that the performance of each individual sub-detector is suitable for capitalizing on the discovery potential of the experiment. This is a challenging task given that the experiment is fundamentally a discovery experiment; therefore, one can

only attempt to quantify sensitivity to discovery – setting a detector specification to enable a discovery of exotic hybrids is fundamentally impossible since the properties and production rates of such hybrids are not known. Furthermore it is anticipated that the limiting factor in many GlueX physics analyses will not be statistics, but instead systematic uncertainties, both experimental and phenomenological in nature. These latter uncertainties will be minimized with more statistics but they do complicate the issue of sensitivity to exotics.

In evaluating detector performance our attention is focused on two key issues:

- signal purity: pure samples of exclusive final states are desirable for amplitude analysis because understanding the nature and structure of background in the context of the amplitude fit is challenging; and
- acceptance: the ability to distinguish between various amplitudes in the fit depends having large angular acceptance.

Beside radiative meson decays, major sources of photons in the GlueX experiment will be mesons that undergo two-photon decays, like $\pi^0$ and $\eta$. Thus, it is important to achieve good invariant mass resolution for these mesons in order to select final states of interest while minimizing backgrounds.

### 5.5.1 $2\gamma$ reconstruction

Below we present some preliminary results on reconstructing both individual $\pi^0$ and $\eta$ decays in addition to a couple of physics channels with multiple neutral particles. In general, our studies are directed at exploring two factors: signal purity and acceptance.

**$\pi^0$ and $\eta$ mass resolution:** To get a preliminary look at mass resolutions, $\pi^0$ and $\eta$ mesons[6] were generated at the center of the target with momentum from 0 to 8 GeV/$c$ and thrown uniformly in full azimuth and up to 90° in polar angle. Figure 5.11 (top) shows the $\gamma\gamma$ invariant mass resolution in the $\pi^0$ (left) and $\eta$ (right) regions when two photons are found in the forward (red), two in the barrel (blue) and one in each calorimeter (purble). The BCAL resolution degrades for high momentum ($>$ 4 GeV/$c$) $\pi^0$'s as merging clusters begin to be an issue; however, we do not expect physics channels to populate the BCAL with $\pi^0$'s of this high momentum. The FCAL aperture sets the lower momentum limit for detecting $\pi^0$'s and $\eta$'s with both photons in the FCAL.

**Selecting $\pi^0$ and $\eta$ candidates:** Since the geometry and resolution of the calorimeters differ, the most effective way to select candidates in particular two-photon channels is by examining either the $\chi^2$ or confidence level of a mass-constrained kinematic fit to a particular decay hypothesis. The fitter provides $\chi^2$ and probability for each meson candidate, as well as fitted momenta of daughter particles. Using a generic sample of MC of the type $\gamma p \to \eta\pi^0 p$, the $\eta$ and $\pi^0$ candidates are selected from all two-photon combinations. Fig 5.12 shows fits to the $\pi^0$ mass of all possible two-gamma combinations when the $\pi^0$ is reconstructed in the FCAL (top), BCAL (middle), and when one photon is found in each detector (bottom). Black histograms

[6]In this simulation the $\eta$ decayed generically into all modes including $\gamma\gamma$. Other decay modes, such as $\pi^+\pi^-\pi^0$ produce some noticeable but non-peaking background in some of the $\eta$ plots.

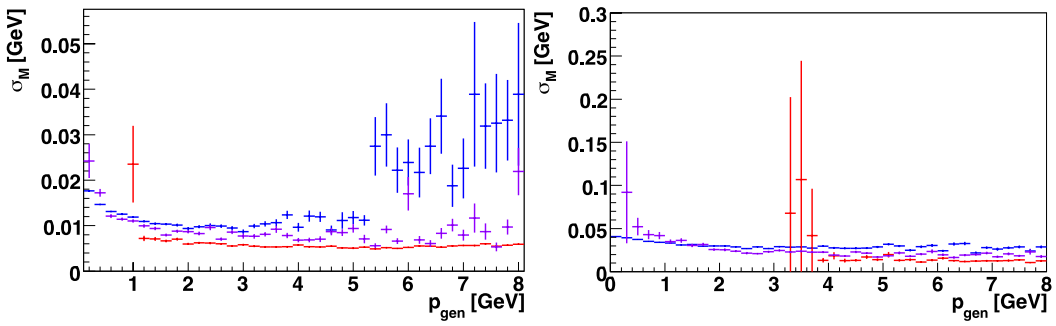


Figure 5.11: Two-photon mass resolution vs. momentum (bottom) for $\pi^0$ (left) and $\eta$ (right) when two photons are reconstructed in the FCAL (red), BCAL (blue), and one photon in each (purple).

on the left show reconstructed two-photon invariant mass, while mass distribution of candidates with $\chi^2 < 5$ (3) are shown by blue (red) histograms. Corresponding confidence levels are shown on the right. The shapes of the backgrounds are driven by kinematics and geometry of the two detectors. For example, in requiring that one The same distributions in the case of $\eta$ fits are shown in Figure 5.13. One can see from the mass plots that selection criteria based on $\chi^2$ is more effective in finding $\pi^0$ and $\eta$ candidates than simple cuts around nominal meson mass as it provides a resolution-dependent cut. The distributions of confidence levels of the left side of Figures 5.12 and 5.13 suggest that the photon error matrix is correctly constructed since combinatoric backgrounds are peaking at low confidence level and the signal appears to be flat in confidence level.

The $\pi^0$ and $\eta$ mass resolutions in Figure 5.12 and 5.13 are summarized in the following table.

| Detector Region | $\sigma(M_{\gamma\gamma})$ for $\pi^0$ [MeV/$c^2$] | $\sigma(M_{\gamma\gamma})$ for $\eta$ [MeV/$c^2$] |
|---|---|---|
| FCAL | 5.4 | 13.2 |
| BCAL | 9.2 | 23.4 |
| FCAL + BCAL | 7.6 | 19.5 |

The noticeable difference between the BCAL and the FCAL resolutions is due primarily to the follow two effects. First, for the physics channel simulated, the BCAL detects on average lower energy photons than the FCAL, and therefore the energy resolution of these photons will be relatively poorer. Second, at high energies, past experimental experience suggests that the "floor" or constant term in the resolution ($B$ in Equation 5.7) dominates. This term, related to systematic errors in reconstruction, is significantly smaller in our MC simulation than has been achievable with actual data in the past. Therefore, at this stage of our simulation, the energy resolution for these higher energy FCAL photons is probably too good.

### 5.5.2 All neutral decay channels

We now focus on exploring reconstruction of a couple of physics channels of the type $\gamma p \to Xp$ where $X$ decays purely into photons. We expect channels of this type to be the most challenging to identify and cleanly separate from background. In what follows, the focus is on the efficiency for reconstructing these signals and

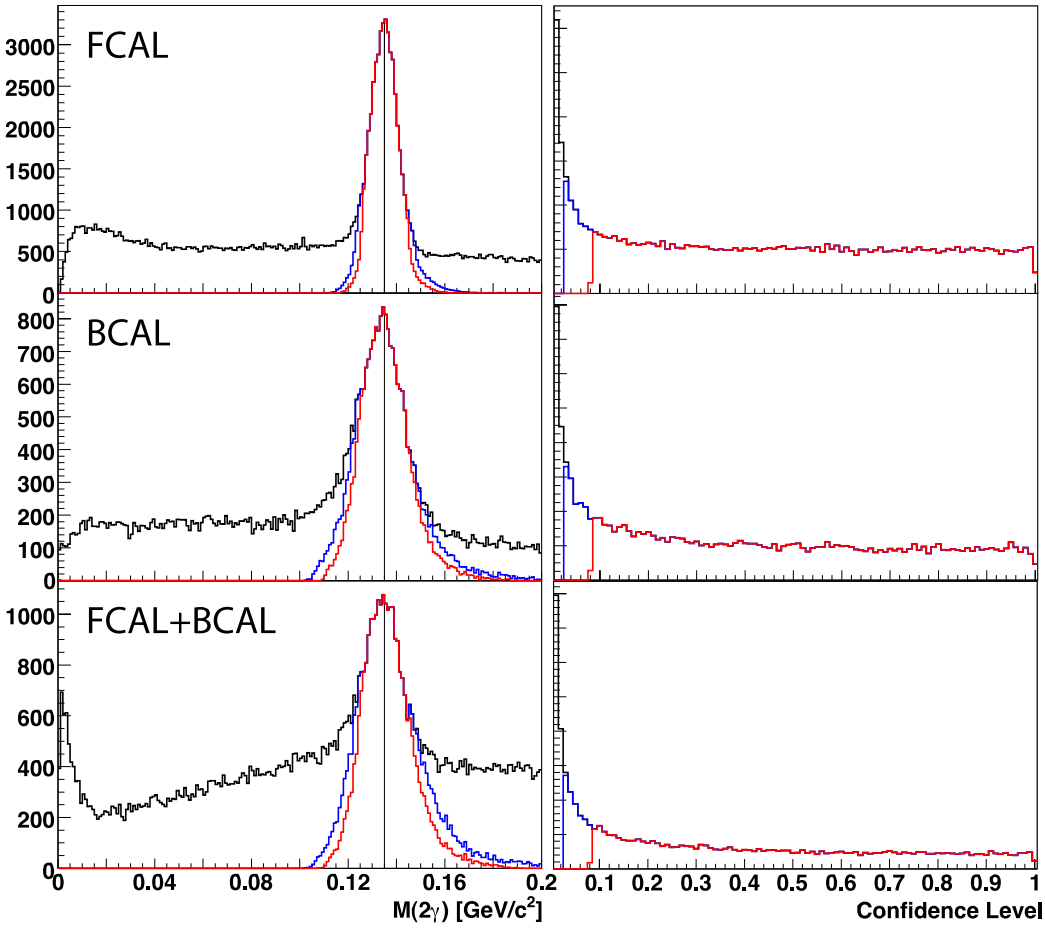


Figure 5.12: Unconstrained invariant mass (left) and fit confidence level (right) for $\pi^0$ candidates after the mass-constrained kinematic fit. Candidates with $\chi^2 < 3$ (5) are shown in red (blue).

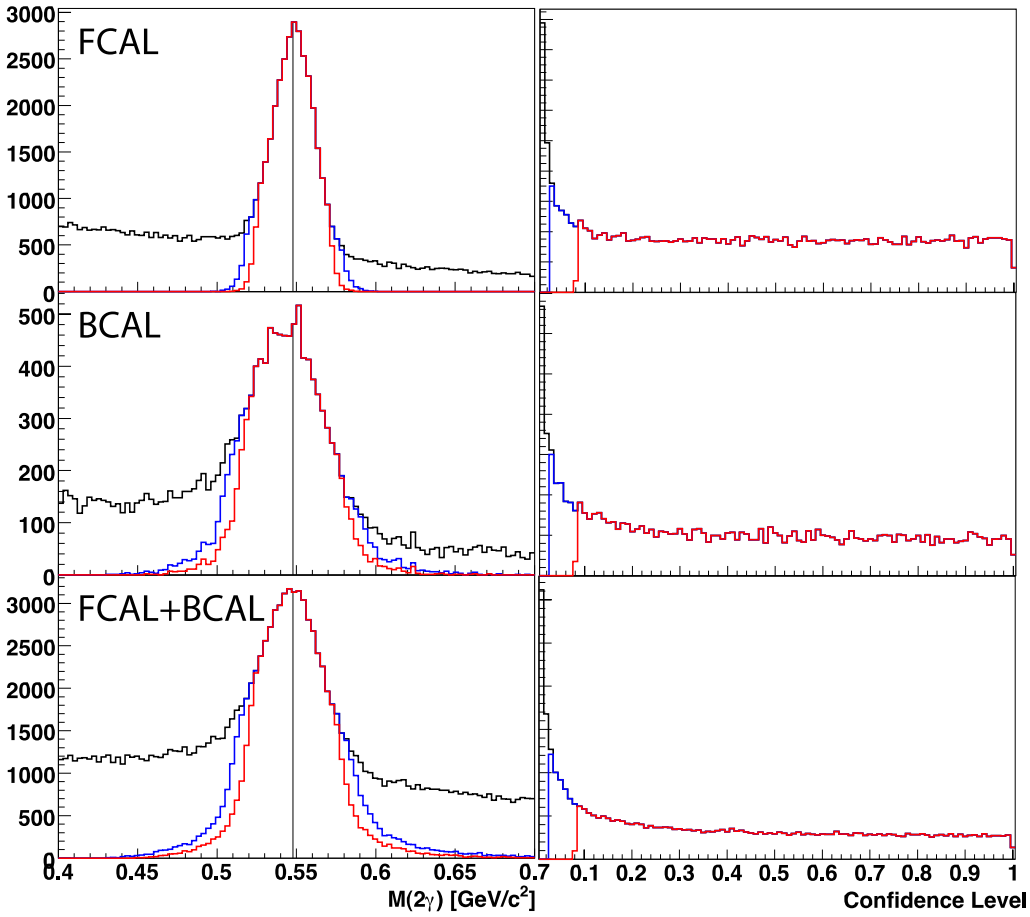


Figure 5.13: Unconstrained invariant mass (left) and fit confidence level (right) for $\eta$ candidates after the mass-constrained kinematic fit. Candidates with $\chi^2 < 3$ (5) are shown in red (blue).

the anticipated background from other hadronic events. To generate background we use a version of PYTHIA tuned to reproduce the known photoproduction cross sections of charged and neutral particles [6]. To ensure that the sample is originates from pure background hadronic photoproduction processes, we examine the identities of the generated particles as provided by PYTHIA and discard events that match our *exclusive* signal final state topology. We then use an independent generator, which allows the incorporation of resonance structure and angular distributions, to generate pure signal events. Of particular interest is the ratio of signal to background efficiency which is key to estimating the sensitivity to signal in particular physics channels.

Theoretical guidance suggests that in photoproduction one might expect exotics to be as prevalent as conventional mesons, but even conventional meson photoproduction cross sections, especially those with large neutral decays, are not well known. We expect the a need to be sensitive to states that have photoproduction cross sections at GLUEX energies at the level of tens to hundreds of nanobarns. Below we outline preliminary results on studies directed at exploring sensitivity to decay channels of interest in search for exotics. To set the scale for the size for the statistical precision of the data set, at peak GLUEX running one expects a physics channel with a cross section of 1 $\mu$b to yield an event rate of approximately 125 Hz.

After selection of a particular channel for analysis one performs a partial wave decomposition or amplitude analysis on the selected set of events to separate the various resonant components that populate a particular final state. Currently there is an effort to develop a framework for carrying out amplitude analysis on distributed computing systems, an ideal solution for the large data sets that will be collected with the GLUEX detector. In the future, we plan to utilize components of this framework to fit mock GLUEX data sets.

**$\gamma p \rightarrow \eta\pi^0 p$:** The first reaction used to study the overall calorimeter performance as well as the ability to reconstruct all-neutral final states was $\gamma p \rightarrow \eta\pi^0 p \rightarrow 4\gamma p$, a relatively simple two-body channel in which observation of exotic states has been claimed [7]. In order to add some structure to the $\eta\pi^0$ system two interfering resonances,$a_0(980) \rightarrow \eta\pi^0$ and $a_2(1320) \rightarrow \eta\pi^0$, were generated with roughly equal amplitudes. For what follows, we only consider the two-photon decay mode of the $\eta$.

For signal events, Figure 5.14 shows multiplicity of all reconstructed photons in both the FCAL and BCAL calorimeter (black histogram) from the sample of 100,000 generated $\gamma p \rightarrow \eta\pi^0 p$ events. In the absence of software to find the recoil proton and extrapolate the trajectory to the calorimeter, we apply a crude algorithm to reject showers from charged particles. All clusters within 0.05 rad of the generated proton polar angle are removed from the list of photons. The blue histogram in Figure 5.14 the resulting photon multiplicity distribution, based on criteria described above. In this case photon distribution peaks at four, which is the expected number of final state photons. The events with higher photon multiplicities result from photon conversion in front of the calorimeters.

Signal $\eta\pi^0$ candidates are selected by requiring that fits to both $\pi^0$ and $\eta$ have $\chi^2 < 3$ and asserting that there are no overlapping photons. The number of selected $\eta\pi^0$ candidates from reaction $\gamma p \rightarrow \eta\pi^0 \rightarrow 4\gamma p$ is shown in Figure 5.15 (left). One sees an average reconstruction efficiency for signal of about 44%. The invariant mass distribution of the signal candidates is shown in Figure 5.15 (right). For comparison the plot is made with both mass-constrained fit (red) and unfit (black) $\pi^0$ and $\eta$ four-vectors. The natural width of the resonances dominates the experimental resolution; therefore, as expected, the kinematic fit only slightly sharpens the peaks.

To understand hadronic background in the $\eta\pi^0$ channel, 1.5 million events were generated by PYTHIA. Based on the total hadronic cross-section of 124 $\mu$b, the cross-section for $\eta\pi^0$ production estimated by PYTHIA is 0.2 $\mu$b, and we use this to provide a rough signal/background normalization.

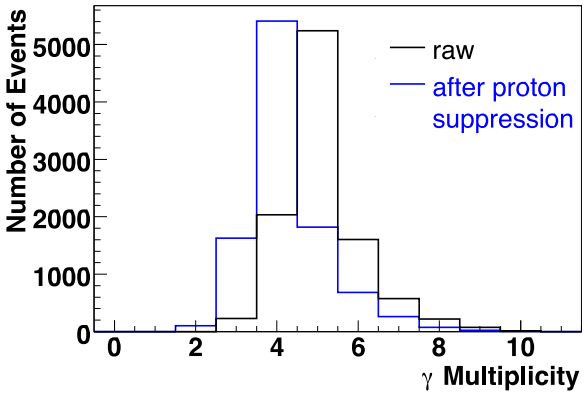


Figure 5.14: Photon multiplicity of all calorimeter showers before (black) and after suppression of proton showers (blue).

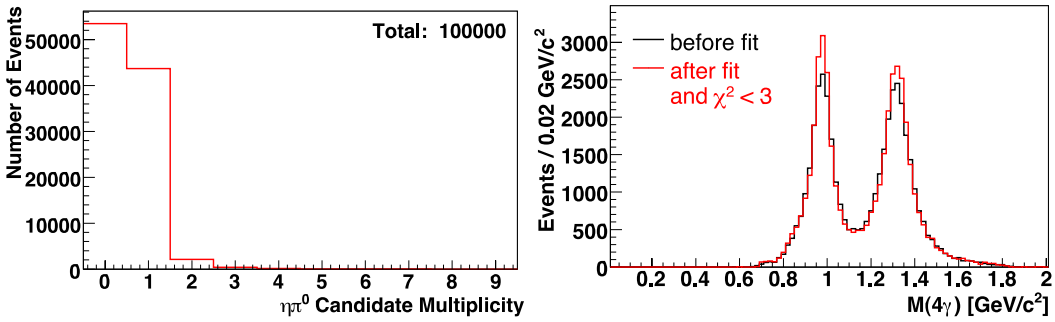


Figure 5.15: Left: $\eta\pi^0$ candidate multiplicity for 100 thousand generated signal events after signal selection requirements are applied. Right: invariant mass distribution of selected candidates before and after the kinematic fit.

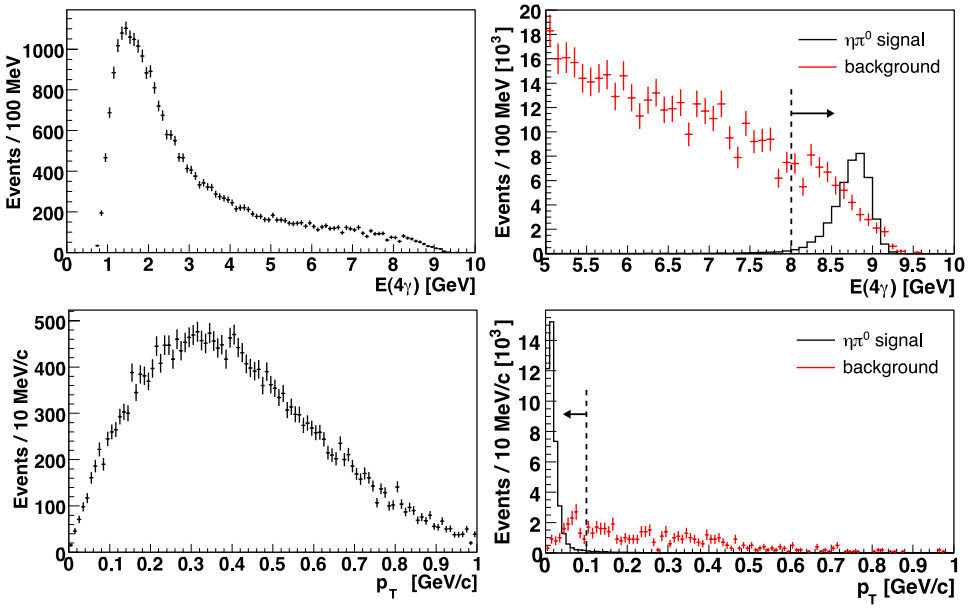


Figure 5.16: Total $\eta\pi^0$ candidate energy (top) and transverse momentum (bottom) for PYTHIA-generated background (left) and signal with scaled background overlaid (right). Backgrounds are scaled with the ratio of cross sections predicted by PYTHIA. Requirements on each variable are indicated by dotted lines and arrows. The plot of transverse momentum is made after the $E(4\gamma)$ requirement.

We suppress background by discarding events with more than five reconstructed photons. Even though our signal channel has just four photons, occasional spurious clusters result in five reconstructed photons, four of which form a suitable signal candidate. After this veto, the number of possible $\eta\pi^0$ candidates from other hadronic reactions is still large. The most effective method of suppressing remaining hadronic backgrounds is to employ a global kinematic fit that enforces four-momentum conservation and evaluate the goodness of fit for the signal candidate; however, such techniques have not yet been fully developed. In lieu of a global kinematic fit, we simply place requirements on the total reconstructed energy and transverse momentum of the signal photons. Figure 5.16 shows the total energy of the $\eta\pi^0$ candidate photons for events with only one candidate from PYTHIA background (top left) and from signal $\eta\pi^0$ (top right). The red points in the top right plot show the background from PYTHIA scaled to the signal based on the ratio of cross sections predicted by PYTHIA. In order to mimic the energy conservation constraint that a full kinematic fit would enforce, we select events with $E(4\gamma) > 8.0$ GeV. In addition, the total transverse momentum $p_{\mathrm{T}}$ must sum to zero to conserve momentum. The lower pair of plots in Figure 5.16 show, in the same style, $p_{\mathrm{T}}$ of the signal $\eta\pi^0$ candidate and recoil proton after the $E(4\gamma)$ requirement. To enforce conservation of momentum, events with $p_{\mathrm{T}} < 100$ MeV/$c$ are selected[7]. For the analyses presented here, we make no additional selection requirements although it is recognized that there exist additional techniques for further suppressing background, *e.g.,* selecting $\pi^0$ or $\eta$ candidates whose decay photon energies are not heavily asymmetric.

Figure 5.17 shows the accepted signal and estimated level of hadronic background for the $\eta\pi^0$ channel assuming a signal production cross section of 0.2 $\mu$b. To improve signal purity one can require exactly four

[7]At this stage, the generated proton momentum is used in the $p_{\mathrm{T}}$ calculation. We expect the resolution in this variable to degrade once the reconstructed proton momentum is used; therefore, we choose to make the requirement significantly looser to avoid overestimating the signal separation power of this variable.

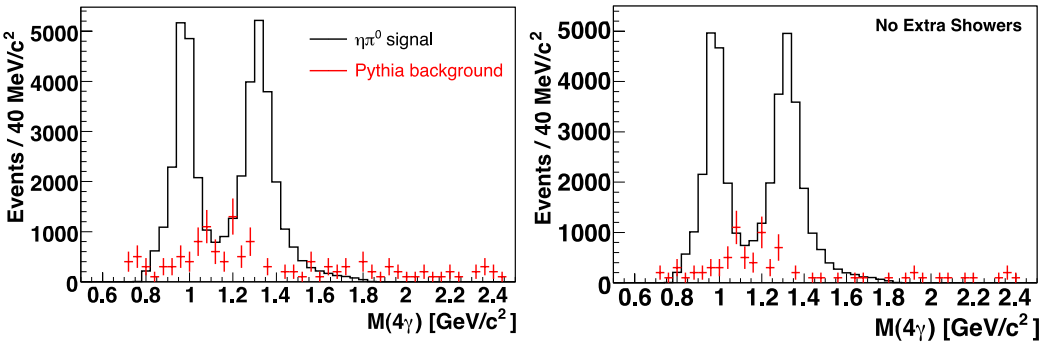


Figure 5.17: The signal from $a_0$ and $a_2$ production in the $\eta\pi^0$ channel (black) compared to the level of expected background (red) assuming a PYTHIA-predicted signal to background cross section ratio of 1:620. The plot on the left allows one extra shower in the event. The plot on the right requires exactly 4 showers.

reconstructed showers in the event. Such a requirement reduces signal efficiency by about 5%. In either case the signal to background is $\geq 10:1$ in the 0.8-1.5 GeV/$c^2$ region, a signal purity that is suitable for amplitude analysis. The expected hadronic background in this channel is significantly smaller in the region around 1.6-2.0 GeV/$c^2$, where one expects a signal for exotics. In this region, we expect to be sensitive at minimum to hybrids produced with cross section of the order of 100 nb with large $\eta\pi^0$ partial width.

**$\gamma p \rightarrow f_1\pi^0 p$:** Another reaction of interest for the GLUEX experiment is the production of states decaying into $f_1\pi^0$, which is predicted by models to be a favorable decay channel for hybrids. The $f_1(1285)$ decays $\approx$50% of the time into the $\eta\pi\pi$ system. It has all-neutral decay mode $\eta\pi^0\pi^0$, which, together with the initial $\pi^0$, results in the final state of eight photons. To reconstruct such a high photon multiplicity state is a challenge, which can provide an insight into GLUEX detector capabilities. A complementary charged mode, $\eta\pi^+\pi^-\pi^0$, is likely to be more efficiently detected and can serve as a cross-check once tracking is better understood.

For this study we create a 200 MeV wide resonance, $X(1800)$, that decays into $f_1\pi^0$. The $f_1$ decay was propagated through the $a_0(980) \rightarrow \eta\pi^0\pi^0$ channel, with $\eta$ undergoing $2\gamma$ decay. The $\eta 3\pi^0$ candidates were selected in a similar way as $\eta\pi^0$ candidates, by requiring that $\chi^2 < 3$ for all candidates and no shared photons. Figure 5.18 shows the number of candidates from a parent sample of 100,000 generated events. The black (red) histogram indicates the candidate multiplicity for the subset of events with 8 or 9 (exactly 8) photons. For this high-multiplicity final state the reconstruction efficiency is between 8-10%.

The estimated $\eta\pi^0\pi^0\pi^0$ photo-production cross-section from PYTHIA is 0.1 $\mu$b, and we use this cross section to scale the background relative to the signal. In order to suppress the background in this channel, we apply the same total energy and transverse momentum requirements as were applied for the $\eta\pi^0$ channel. Figure 5.19 shows the $\eta\pi^0\pi^0\pi^0$ invariant mass for signal (black) and expected hadronic background (red) for events with one extra shower (left) and exactly 8 showers (right). Because of the high shower multiplicity, the signal purity is enhanced notably by requiring exactly 8 showers be reconstructed in the detector. Although the statistical precision on the background at this stage is poor, this requirement improves the signal to background ratio to about 5:1 in the signal region suggesting sensitivity to hybrids produced at the level of 100 nb with large $f_1\pi$ partial widths.

We have presented preliminary results from advanced physics simulations that begin to address the ability

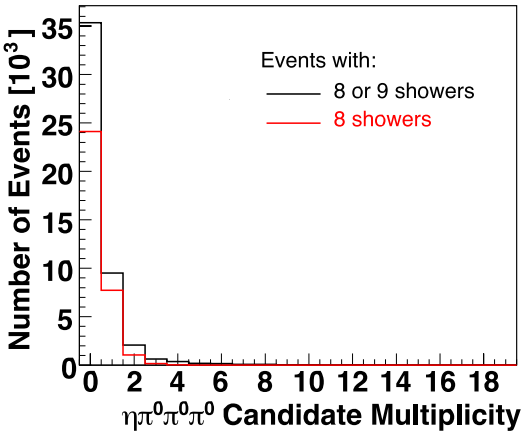


Figure 5.18: $\eta\pi^0\pi^0\pi^0$ candidate multiplicity for events with 8 or 9 (exactly 8) showers is shown in black (red). The parent sample from which these subsets were derived consisted of 100,000 generated events.

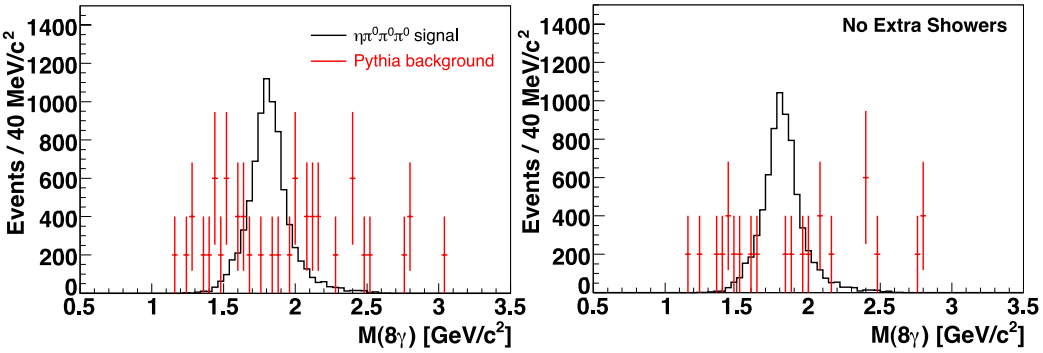


Figure 5.19: A characteristic resonance signal in the $f_1\pi^0$ channel (black) compared to the level of expected background (red) assuming a PYTHIA-predicted signal to background cross section ratio of 1:1240. The plot on the left allows one extra shower in the event. The plot on the right requires exactly 8 showers.

of the GlueX calorimetry system to cleanly identify a wide variety of final states. While it is difficult to develop a quantitative figure of merit for physics performance or discovery potential it is encouraging to see, for example, that clean reconstruction of many-photon final states produced with cross sections of a hundred nb seems to be feasible. These studies will be extended to include charged particles, where we expect our sensitivity to increase, and will be refined as our understanding of physics backgrounds and models for hybrid production improve.

### 5.5.3 Amplitude Analysis

Discovery of hybrid mesons depends not only on the ability to cleanly identify their decay products but also to utilize an amplitude analysis to separate broad exotic resonances from conventional states. Amplitude analysis (or partial wave analysis) attempts to fit a set of interfering resonances amplitudes to the angular distribution of decay products observed in the detector. Since the technique utilizes the angular information available in the decay and is sensitive to interference and relative phases of amplitudes it is a powerful tool for detecting and unambiguously identifying the quantum numbers of broad resonances. However; in order to minimize systematic errors it is essential that the experimental acceptance be well understood – this is achieved with an accurate simulation.

Significant work has already gone into developing amplitude analysis tools and techniques for GlueX. A subset of the collaborators have secured funding through the NSF Physics at the Information Frontier program to develop techniques to carry out this high-statistics computationally intensive analysis on distributed clusters or computers. Currently tools to generate Monte Carlo with appropriate angular distributions and to do preliminary amplitude analysis exist. Figure 5.20 shows on the left the characteristic angular distribution of $a_0$ and $a_2$ in the Gottfried-Jackson frame for the signal $\eta\pi^0$ sample discussed in detail above. The plot on the right side of Figure 5.20 shows, as proof of principle, a preliminary fit to these mock data in which the fitter separates the $S-$ and $D-$wave components associated with $a_0$ and $a_2$ states, respectively. A resonant $P$-wave $\eta\pi^0$ state is exotic. Of particular interest in future studies will be understanding cross-feed in the fit from non-exotic states into these exotic waves as we vary our assumptions about our acceptances, especially in the key region between the barrel and forward calorimeters, as it is possible for systematic errors in acceptance to manifest themselves in the form of false signals in the amplitude analysis.

## 5.6 Summary

In summary a detailed simulation and reconstruction algorithm for both the barrel and forward calorimeters of the GlueX experiment has been developed with input from beam tests and other studies conducted with actual detector hardware. This simulation permits one to carryout prototype physics analyses on mock data sets that enable a wide variety of studies including exploring the effect of detector material and geometry on acceptance, understanding hadronic backgrounds in physics channels, and probing systematic errors in amplitude analysis. As has been mentioned above, quantitative figures of merit for exotic meson discovery are difficult to develop; however, from the preliminary studies, we conclude that the design and performance of the GlueX calorimetry preserves the potential for discovery in high-multiplicity neutral final states.

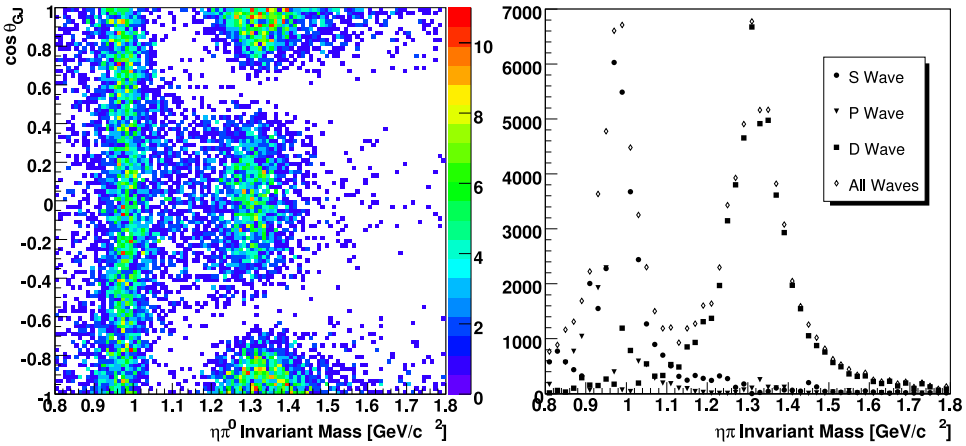


Figure 5.20: (left) $\cos\theta$ of the $\eta$ in the Gottfried-Jackson frame as a function of the $\eta\pi^0$ candidate invariant mass for signal Monte Carlo. The characteristic spin-zero and spin-two structures of the $a_0$ and $a_2$ are evident. (right) Fit results of a preliminary partial wave decomposition simulated $a_0$ and $a_0$ production in the $\eta\pi^0$ channel. In general, the fitter correctly separates the $S$- and $D$-wave structures.

# References

[1] B. Leverington. Sampling fraction fluctuations. Technical report, GlueX Collaboration, 2007. GlueX-doc-827-v3.

[2] R. T. Jones et al. A bootstrap method for gain calibration and resolution determination of a lead-glass calorimeter. *Nucl. Instrum. Meth.*, A566:366–374, 2006.

[3] R. T. Jones et al. Performance of the RADPHI detector and trigger in a high rate tagged photon beam. *Nucl. Instrum. Meth.*, A570:384–398, 2007.

[4] W.-M. Yao et al. Review of particle physics. *J. Phys.*, G33:1, 2006.

[5] M. Adinolfi et al. Calibration and reconstruction performances of the KLOE electromagnetic calorimeter. *Nucl. Instrum. Meth.*, A461:344–347, 2001.

[6] T. Sjöstrand, S. Mrenna, and P. Skands. Pythia 6.4 Physics and Manual. Technical report, Lund University, 2006. hep-ph/0603175 and http://www.thep.lu.se/~torbjorn/Pythia.html.

[7] A. Abele et al. Evidence for a $\eta\pi$ P-wave in $\bar{p}p$ annihilations at rest into $\pi^0\pi^0\eta$. *Phys. Lett.*, B446:349–355, 1999.